Check for updates

Technical Notes

Inertial Inflation and Correction of Control Effectiveness from Wind Tunnel Dynamic Excitations

Burhanuddin Saify,* Coen de Visser,† and Xuerui Wang‡
Delft University of Technology, 2629 HS Delft, The Netherlands

https://doi.org/10.2514/1.G009651

Downloaded by Technische Universiteit Delft on September 21, 2026 | http://arc.aiaa.org | DOI: 10.2514/1.G009651

Nomenclature

A	=	regressor matrix
A_k	=	amplitude of the kth multisine component, deg
C_L	=	lift coefficient
$C_{L_{SS}}$	=	quasi-steady lift coefficient
$C_{L_{\delta_i}}$	=	lift control effectiveness for control surface with index i, 1/deg
c	=	damping, N s/m
c_r	=	root chord, m
F_b	=	balance force measurement, N
k	=	stiffness, N/m
L	=	lift force, N
m	=	mass, kg
T	=	period of a multisine input, s
U_∞	=	freestream velocity, m/s
x_i	=	state i of the state-space model
$\boldsymbol{y}$	=	observation vector
δ_e	=	elevator deflection, deg
δ_i	=	deflection of control surface i, deg
$\boldsymbol{\theta}$	=	parameter vector
$\boldsymbol{\xi}_i$	=	regressor column vector
σ	=	standard deviation
ϕ_k	=	phase of the kth multisine component, rad

Subscripts

b	=	force balance
t	=	mounting table
w	=	wing

Presented as Paper 2025-0005 at the AIAA SciTech 2025 Forum, Orlando, FL, January 6–10, 2025; received 7 October 2025; accepted for publication 8 April 2026; published online 5 May 2026. Copyright © 2026 by Burhanuddin Saify, Coen de Visser, and Xuerui Wang, Delft University of Technology. Published by the American Institute of Aeronautics and Astronautics, Inc., with permission. All requests for copying and permission to reprint should be submitted to CCC at www.copyright.com; employ the eISSN 1533-3884 to initiate your request. See also AIAA Rights and Permissions https://aiaa.org/publications/publish-with-aiaa/rights-and-permissions/.

*Ph.D. Candidate, Aerospace Structures and Materials Department, Faculty of Aerospace Engineering, Kluyverweg 1; b.saify@tudelft.nl. Member AIAA.

†Associate Professor, Control & Operations Department, Faculty of Aerospace Engineering, Kluyverweg 1; c.c.devisser@tudelft.nl. Member AIAA.

‡Assistant Professor, Dual Affiliation at the Department of Control and Operations and the Department of Aerospace Structures and Materials, Faculty of Aerospace Engineering, Kluyverweg 1; x.wang-6@tudelft.nl. Senior Member AIAA (Corresponding Author).

I. Introduction

THE determination of control surface effectiveness through flight test data or wind tunnel data is a critical component of aircraft aerodynamic model identification. Exciting the dynamics of the aircraft is an important system identification step achieved through specially designed control surface inputs. Data gathered from these maneuvers are used to fit models that parameterize the aerodynamic properties of the aircraft into physically interpretable coefficients such as the lift slope C_{L_α}, pitch damping C_{m_q}, and aileron control effectiveness $C_{l_{\delta_a}}$.

Common excitation inputs used for aircraft system identification include doublets and multistep maneuvers such as 3211 maneuvers [1]. These inputs are effective for conventional tube–wing aircraft configurations with standard elevator, aileron, and rudder control surfaces. Elevator doublets are used to excite longitudinal dynamics, for example, and aileron or rudder doublets to excite the lateral dynamics. For aircraft with numerous distributed control surfaces, such as flying wings, standard step-based inputs can be inefficient in terms of testing time, since control surfaces are excited one at a time or in pairs. Multisine excitations are a type of excitation where all control surfaces deflect simultaneously and sinusoidally with practically no input correlation. Therefore, the dynamics of the aircraft can be efficiently excited for system identification through these maneuvers. This enables the measurement of individual control surface contributions to aerodynamic forces, even when multiple surfaces are deflected simultaneously [2–4]. Additionally, control surface interactions can also potentially be modeled through multisines if such an effect is significantly present [5]. Multisines have been used for system identification of conventional aircraft configurations [6] as well as flying wings with distributed control surfaces [7,8].

While often used in flight testing, multisine excitations are also potentially useful in the wind tunnel during the early phases of aircraft development. The common approach to measuring control effectiveness (CE) in the wind tunnel is to statically deflect surfaces or surface groups (such as elevators and ailerons) one at a time and measure the resulting aerodynamic forces. This approach is more time-consuming and does not capture dynamic phenomena, such as those arising from unsteady aerodynamic effects, which may be significant for fast control surface deflections. Using multisines for CE estimation in the wind tunnel before flight testing enables the isolation and analysis of dynamic effects that are not associated with the rigid-body motion of the flight vehicle, such as short period and Dutch roll, and that could therefore contaminate them if left unaccounted for. Therefore, by reducing testing time and allowing dynamic effects to be captured, multisines can be beneficial for wind tunnel testing, especially when leading up to flight testing.

Existing literature on the use of multisine excitations to identify control surface effectiveness parameters in wind tunnel testing is sparse. Heeg et al. [9] applied multisine inputs to an aeroelastic wind tunnel model and noted their time efficiency. Ertveldt et al. [10] used multisines to excite pitch and plunge motions of a 2D airfoil section in a wind tunnel. However, to the best of the authors' knowledge, no comprehensive study has compared dynamic control surface excitations such as multisines with static deflections for CE identification in a wind tunnel setting.

To address this gap, the current study investigates the use of multisine excitations to identify CE on a flying wing platform in a wind tunnel, with results compared to those from static deflections. While differences between the two approaches were anticipated, the primary objective was to quantify the nature and extent of these discrepancies. It was hypothesized that CE estimates would decrease with increasing excitation frequency due to unsteady aerodynamic

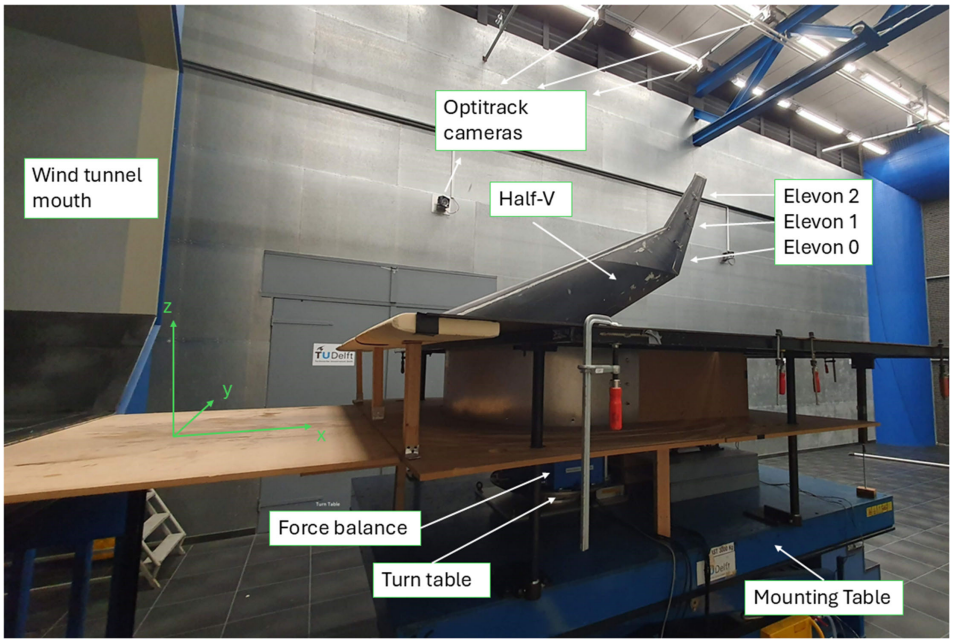


Fig. 1 Experimental setup of the Half-V.

effects. As the control-surface excitation frequency increases, the aerodynamic response is expected to deviate from its quasi-static value because the circulation and wake cannot adjust instantaneously to the imposed motion. In unsteady aerodynamics, part of the lift is generated with a time delay associated with vorticity shedding and convection, which produces both amplitude attenuation and phase lag relative to the quasi-static response [11,12]. Consequently, the control effectiveness is generally expected to decrease with increasing reduced frequency.

Wind tunnel testing was conducted at the Open Jet Facility at TU Delft.[§] The flying wing wind tunnel model, referred to hereafter as the Half-V, was a good platform for this study because it features three independently controlled elevons. However, the results of the initial wind tunnel tests revealed unreported dynamic phenomena that contradicted expected behavior. Rather than decreasing with increasing excitation frequencies due to unsteady aerodynamic effects, the control effectiveness estimates for each of the elevons appeared to increase with excitation frequency. As a specific example, a 12% inflation in the parameter $C_{L_{\delta_e}}$ (elevator lift CE) was observed when estimated from data where control surfaces were sinusoidally deflected at 2.5 Hz when compared to the quasi-static parameter value obtained at 0.5 Hz. Therefore, the dynamic effects were significant and led to an apparent increase in CE with frequency. This apparent increase in CE estimates with control surface deflection frequency is termed "control effectiveness inflation" in this paper. The CE inflation effect was hypothesized to manifest from inertial forces due to wing vibrations corrupting the measurements.

The inflation of CE parameter estimates with control surface excitation frequency is a concern if dynamic excitations such as multisines are to be used for system identification of a wing or an aircraft in a wind tunnel because it may lead to incorrect design conclusions on control surface sizing and control system design and tuning. To the best of the authors' knowledge, this problem has not been formally addressed in previous work. Therefore, the first contribution of this work is to expose CE inflation and quantify its implications for testing with dynamic control surface excitations. An in-depth investigation was conducted into the source of the discrepancy between the wind tunnel results and unsteady aerodynamic theory. The second contribution presents a validated methodology to correct dynamic force-balance measurements, enabling more accurate estimates of CE from time-efficient dynamic control surface excitations in a wind tunnel setting.

The remainder of this paper is organized into three parts. First, the general methodologies for experimentation and parameter estimation are presented in Sec. II. The investigation of the parameter inflation phenomenon is presented in Sec. III, followed by the proposed measurement correction methodology in Sec. IV. A discussion of the methodology and its applicability is presented in Sec. V. Finally, the paper is concluded in Sec. VI.

II. Control Effectiveness Identification Methodology

A wind tunnel experiment was conducted where several control surface excitations were tested, both in static and dynamic settings. The data from this experiment were analyzed and processed to identify CE estimates. This section describes the test setup, parameter estimation methodology, and the control surface excitations employed.

A. Wind Tunnel Setup

The experiments were conducted in the Open Jet Facility (OJF) at TU Delft, a large low-speed wind tunnel capable of producing steady flow speeds up to 35 m/s. The tunnel features a 2.85 m × 2.85 m nozzle cross section. In this study, all tests were performed at a freestream velocity of 25 m/s.

The experimental configuration is shown in Fig. 1. It consists of the wing (Half-V) test article mounted on a structural frame within the tunnel. The model is attached to a six-component force balance, which is itself mounted on a motorized turntable. The turntable allows adjustment of the wing's incidence angle relative to the oncoming flow. Forces and moments are sampled at 2 kHz and recorded to a computer.

Input excitation signals are generated using an Arduino Uno microcontroller[¶] located onboard the Half-V. These signals are sent directly to the elevon servos. Each servo shaft is mechanically linked to a potentiometer that directly measures the deflection angle of the servo shaft. Due to nonlinearities in the linkage kinematics, third-order polynomial calibration curves were developed to map potentiometer readings to surface deflection angles. The Arduino samples each potentiometer signal at approximately 100 Hz, converts the analog data to digital form, and transmits it to a computer via a serial connection for logging.

[§]https://www.tudelft.nl/lr/organisatie/afdelingen/flow-physics-and-technology/facilities/low-speed-wind-tunnels/open-jet-facility.

[¶]https://store.arduino.cc/products/arduino-uno-rev3.

Downloaded by Technische Universiteit Delft on September 21, 2026 | http://arc.aiaa.org | DOI: 10.2514/1.G009651

Downloaded by Technische Universiteit Delft on September 21, 2026 | http://arc.aiaa.org | DOI: 10.2514/1.G009651

B. Parameter Estimation

An ordinary least squares (OLS) estimator was used to estimate CE parameters from the wind tunnel data gathered using the different control surface excitation methods. The model structure is shown in Eq. (1), where the lift coefficient is a function of the deflections δ_i, $i = 0, 1, 2$, of the elevons. The index 0 refers to the inboard elevon, 1 to the middle elevon, and 2 to the outboard elevon. The parameters to be determined for this linear model are the CE terms corresponding to each elevon $C_{L_{\delta_i}}$, $i = 0, 1, 2$, which physically represent the contribution of each elevon to producing aerodynamic lift. Dynamic derivatives such as C_{L_q} are not included in the model, as dynamic motions of the complete wing were not excited. Additionally, the results shown in this paper are for a single angle of attack (0 deg); hence, the C_{L_α} parameter is also omitted.

$$C_L = C_{L_0} + C_{L_{\delta_0}}\delta_0 + C_{L_{\delta_1}}\delta_1 + C_{L_{\delta_2}}\delta_2 \tag{1}$$

The explanatory variables for the OLS estimator are the measured angles of the control surfaces (δ_i), and the modeled variable is the measured nondimensionalized lift coefficient. A linear-in-the-parameters polynomial model, Eq. (2a), is used to model the dependent variable $\boldsymbol{y} \in \mathbb{R}^n$ with regressors $\boldsymbol{\xi_i}$ in $A = [\mathbf{1} \quad \boldsymbol{\xi_1} \quad \boldsymbol{\xi_2} \quad \ldots \quad \boldsymbol{\xi_p}] \in \mathbb{R}^{n\times p}$, model parameters $\boldsymbol{\theta} \in \mathbb{R}^p$ and residuals $\boldsymbol{\epsilon} \in \mathbb{R}^n$. The optimal parameters $\hat{\boldsymbol{\theta}}$ are determined using Eq. (2b). The parameter variance–covariance matrix is calculated using Eq. (2c), where σ^2 is the variance of the residuals [1].

$$\boldsymbol{y} = A\boldsymbol{\theta} + \boldsymbol{\epsilon} \tag{2a}$$

$$\hat{\boldsymbol{\theta}} = (A^T A)^{-1} A^T \boldsymbol{y} \tag{2b}$$

$$\mathrm{Cov}(\hat{\boldsymbol{\theta}}) = \sigma^2 (A^T A)^{-1} \tag{2c}$$

The modeled variable, $\boldsymbol{y}$, in this case is C_L; the parameter vector is $\boldsymbol{\theta} = [C_{L_0} \quad C_{L_{\delta_0}} \quad C_{L_{\delta_1}} \quad C_{L_{\delta_2}}]^{\mathrm{T}}$; and the regressor matrix is $A = [\mathbf{1} \quad \boldsymbol{\delta_0} \quad \boldsymbol{\delta_1} \quad \boldsymbol{\delta_2}]$, where the first column vector is the bias, and the remaining vectors correspond to the deflections of the control surfaces, which are inputs to the model.

C. Multisine Excitations

Multisine excitations are a sum of sinusoids covering a set of prescribed frequencies with associated amplitude and phase. Every control surface receives a distinct multisine command signal simultaneously. The frequencies of the individual sine waves are distributed among the control surfaces such that the deflection correlation for any control surface pair is zero. Equation (3) is used to define the instantaneous deflection δ_i of control surface i as a function of time, where T is the period, n is the total number of frequencies, A_k is the amplitude, and ϕ_k is the phase [3]. A uniform amplitude spectrum was used, while the phase angles were set using Eq. (4) [1].

$$\delta_i(t) = \sum_{k\in\{1,2,\ldots,n\}} A_k \sin\left(\frac{2\pi k t}{T} + \phi_k\right) \tag{3}$$

$$\phi_k = \phi_{k-1} - \frac{\pi k^2}{n} \qquad k = 2, 3, \ldots, n \tag{4}$$

The multisine deflections performed during the wind tunnel testing campaign were varied by adjusting the maximum frequency and the signal amplitude. A multisine frequency of around 2.5 Hz was considered sufficient to cover the rigid-body aerodynamic modes of the scaled flight testing article based on this wing [13], on which these excitations will be employed in future system identification flight tests. However, since the servos achieve an actuation frequency up to 3.6 Hz, multisine excitations were also tested at this maximum frequency for exploratory reasons. The period T was chosen to be 5 s for all the multisine tests because it offers a sufficient frequency resolution of 0.2 Hz. The frequencies were assigned sequentially to each elevon to ensure a uniform spectral distribution over the surfaces. The same 5 s segment was repeated 10 times per maneuver to allow phase averaging of the signal.

The amplitude spectra of the lift coefficient and control surface deflections from a test run are shown in Fig. 2, with the corresponding time series for the control surface deflection angles shown in Fig. 3. Each elevon was assigned four distinct excitation frequencies, collectively spanning a frequency range from 0.4 to 2.6 Hz. As is evident in the lift coefficient spectra, the aerodynamic response is concentrated at the same frequencies as the control surface excitations. The relative magnitudes of the spectral peaks reflect the size differences among the elevons: the inboard elevon, being the largest, produces the highest peaks; the outboard elevon, the smallest, results in the lowest peaks; and the central elevon yields intermediate responses. Figure 2 also shows the subtle increase in the frequency peaks of the measured lift coefficient with frequency, which manifests as increased CE parameter estimates. The time series measurements for the lift coefficient are shown in Fig. 4.

D. Static Tests

The CE parameters estimated from static deflections serve as a quasi-static ground-truth reference for comparison with the estimates obtained using multisine inputs and stepped-sine inputs. Static deflection tests were conducted in which each elevon was simultaneously held at a fixed angle for 5 s. The deflection angles ranged from −10 to +10 deg in 5 deg increments, resulting in 125 total combinations across the tested elevons. Each static maneuver sequence lasted approximately 10 min, in contrast to the 50 s duration of a typical multisine excitation run. It is noted that since the wing exhibits static aeroelastic deformation under control-surface loading, the resulting reference values inherently include

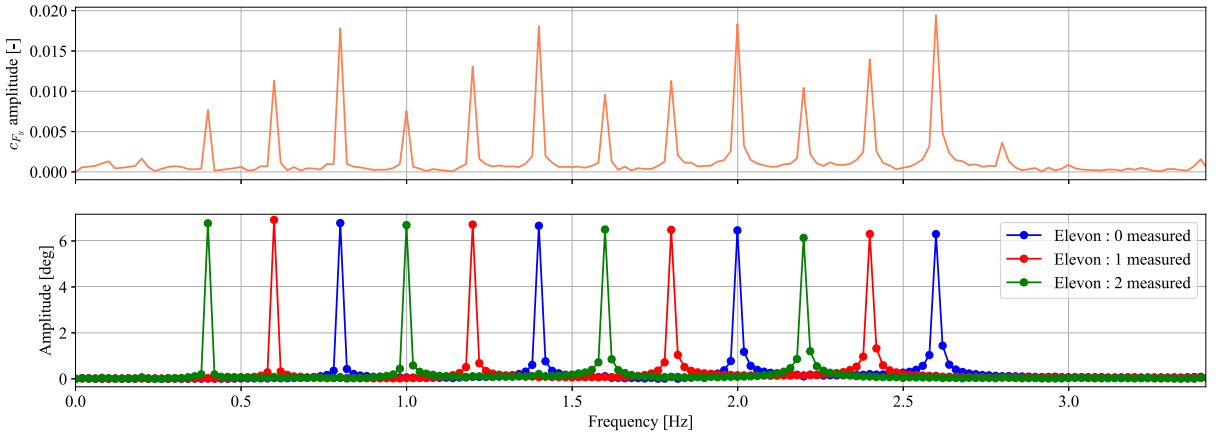


Fig. 2 Amplitude spectra of the measured lift coefficient and deflections of each elevon for a multisine excitation.

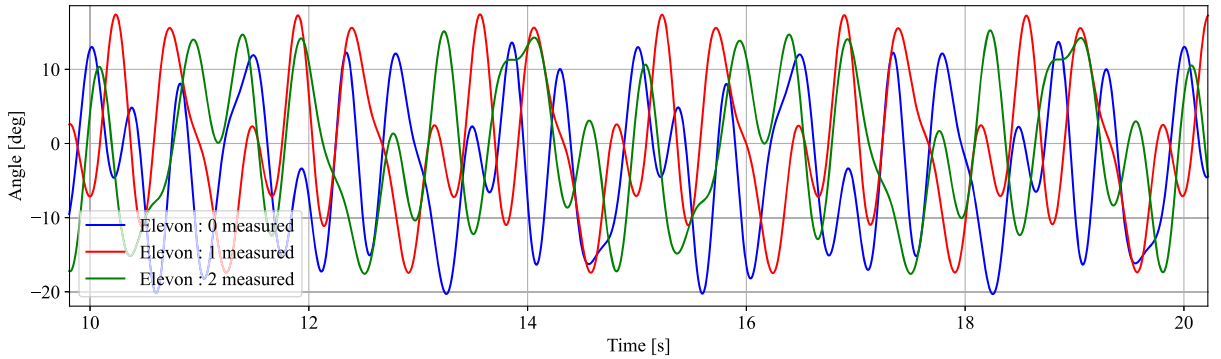


Fig. 3 Control surface deflection angles measured for a multisine excitation.

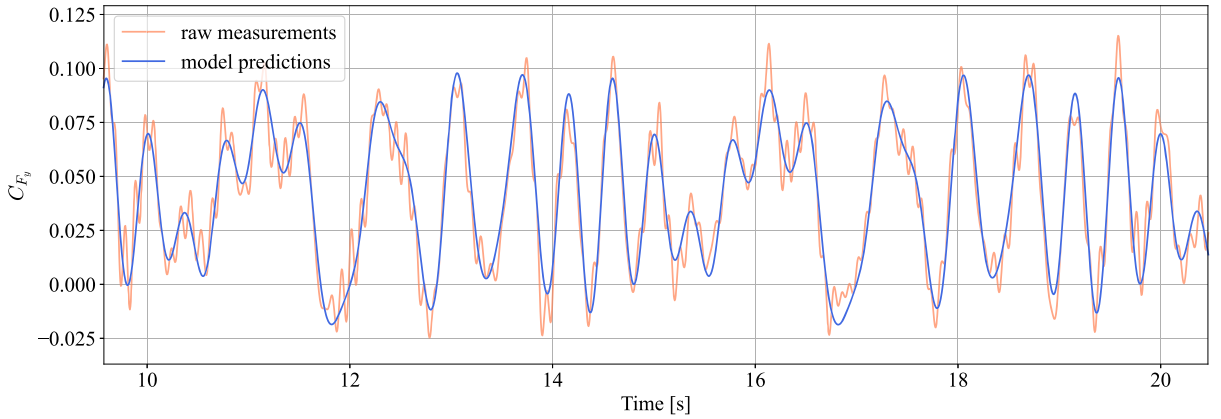


Fig. 4 Measured normal force coefficient time series data for multisine excitations with model predictions.

Downloaded by Technische Universiteit Delft on September 21, 2026 | http://arc.aiaa.org | DOI: 10.2514/1.G009651

the static elastic response of the configuration. Nevertheless, they provide the most appropriate baseline for comparison with the dynamically excited measurements, since they are not affected by dynamic inertial contamination.

E. Stepped Sines

In addition to the static deflections and multisine inputs, discrete sine sweep excitations were also employed because specific frequencies can be tested through these excitations, while multisines excite a range of frequencies simultaneously. In this case, all three elevons were actuated in unison, meaning that the individual CE contributions of each surface could not be independently identified. Instead, the resulting estimates represent a combined, equivalent single elevon. The primary objective of these inputs was to investigate whether, and how, CE varies with the frequency of excitation. The sine sweep consisted of sequential 10 s intervals at fixed frequencies, ranging from 0.5 to 2.5 Hz in 0.25 Hz increments. It may be noted that the highest frequency tested in the stepped-sine excitation was 2.5 Hz, which is lower than the maximum frequency of 3.6 Hz employed in the multisine excitation. This decision was made primarily for safety considerations. During multisine excitation, the control surfaces move in a way that partially offsets their combined effect, whereas during stepped-sine excitation they move in unison. Since the 3.6 Hz multisine excitation was already found to induce significant wing deformation, higher frequencies were not considered in the stepped-sine tests in order to mitigate the risk of structural failure. Additionally, excitations up to 2.5 Hz meet the initial goal of covering the frequency range of interest for this aircraft.

III. Parameter Inflation Phenomenon and Analysis

The results of parameter estimation using the two dynamic excitations, multisines and stepped sines, are presented here, as well as how they compare to CE estimates from static data. The parameter inflation phenomenon, which arises from inertial forces, is also explained, along with the expected unsteady aerodynamic behavior and CE estimates expected from indicial response theory.

A. Multisine Parameter Estimation Results

The initial results of identifying CE parameters using multisine excitations are shown in Fig. 5. The subplots show CE values for the inboard, middle, and outboard elevons from left to right, respectively. Each point along the horizontal axis corresponds to a distinct experimental run, with the vertical axis showing the associated parameter estimate obtained through the OLS estimator.

The CE parameter inflation is evident, with estimates from multisine excitations significantly exceeding those derived from static deflection data. The influence of multisine excitation frequency is also evident, with higher-frequency inputs (e.g., 3.6 Hz) yielding larger CE estimates than those obtained using lower-frequency multisines around 2.6 Hz. The error bars for the multisine-derived CE estimates are larger than those for the static estimates because each static run lasted approximately 10 min, compared to only 50 s for a multisine run, resulting in a significantly larger number of samples for the static case and, therefore, lower parameter variances as per Eq. (2c).

B. Parameter Variance with Frequency

The multisine excitation-derived CE parameter estimates indicate an apparent increase in CE values with maximum multisine excitation frequency. However, there is a lack of detail in how the CE parameter estimates vary with excitation frequency. Therefore, stepped-sine excitations were also performed as part of the experimental campaign. While these offer better frequency resolution, the three elevons move as one unit. Therefore, the CE is estimated for an equivalent single elevon with deflection δ_e. In this case, the regressor matrix is simply $A = [\mathbf{1} \quad \boldsymbol{\delta_e}]$, and the parameter vector is $\boldsymbol{\theta} = [C_{L_0} \quad C_{L_{\delta_e}}]^{\mathrm{T}}$.

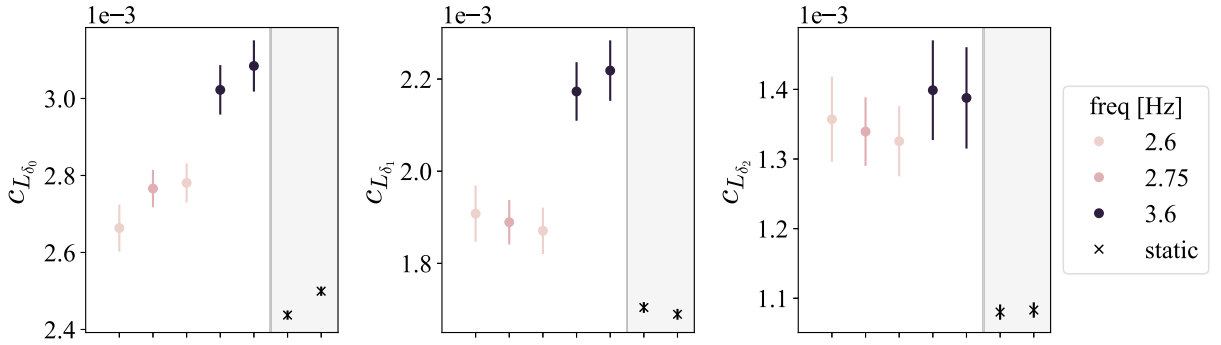


Fig. 5 CE parameters estimated through multisines at varying maximum frequencies and static deflections.

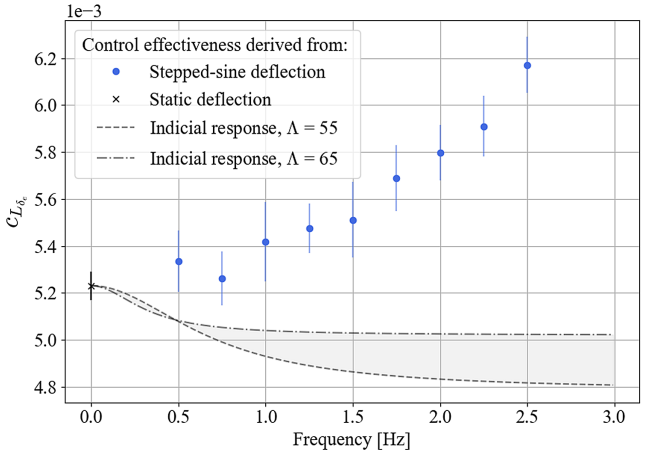


Fig. 6 Variation of CE with excitation frequency.

This is not a problem, since the purpose of these excitations was to analyze the CE–frequency relationship for a control surface that is dynamically excited at a single frequency. The CE parameter estimated for the equivalent single elevon is just the sum of the individual CE values of the three individual elevons.

Figure 6 shows the CE parameter inflation phenomenon observed during the stepped-sine dynamic excitations of the elevons. The error bars cover 3 standard deviations estimated through OLS. It is clear from this figure that the CE parameters exhibit an apparent increase in value with the frequency of control surface excitation.

C. Expected Unsteady Control Effectiveness Measurement

Theoretical results in unsteady aerodynamics for inviscid incompressible flow, such as those of Theodorsen [11] and Wagner [12], predict that the lift-generating effectiveness of an airfoil decreases when it is oscillating in pitch. Wagner offers convenient indicial functions that can be used directly in the time domain to predict lift evolution with a step change in angle of attack. However, in this case, we wanted to estimate the theoretical lift response due to an oscillating control surface on a highly swept 3D wing.

Queijo et al. [14] have extended the 2D indicial function model to obtain approximate indicial functions for the dynamic lift response of tapered, swept wings in incompressible flow. They employ a closed vortex system that involves a swept vortex fixed at the wing, with trailing vortices at the wing tips that finally connect to a swept shed vortex that convects downstream at half the freestream velocity. Consequently, a complex vortex wake is replaced by a single, swept, shed vortex filament. The indicial function shown in Eq. (5) models the ratio of the dynamic lift coefficient $\Delta C_L(t)$ to the quasi-steady lift coefficient $C_{L_{ss}}$, where U_∞ is the freestream velocity, c_r is the wing root chord, t is time, and y and z are parameters that shape the indicial response and depend on geometric wing parameters such as aspect ratio, taper ratio, and quarter-chord sweep. The quasi-steady step in lift coefficient can come from either an angle-of-attack change or a control surface deflection. In this case, we are interested in the latter.

$$\frac{\Delta C_L(t)}{C_{L_{ss}}} = 1 - ye^{-z\left[\frac{2U_\infty t}{c_r}\right]} \tag{5}$$

The Half-V is a highly swept wing; however, it contains two kinks along the span, resulting in a sweep angle that changes with spanwise location. An equivalent quarter-chord sweep was estimated for the Half-V by taking an area-weighted average of the quarter-sweep angles at the three regions of the wing, resulting in a value of 60 deg. The aspect ratio is 5, and the taper ratio is 0.13. This results in values of 0.057 and 0.540 for y and z, respectively.

It is important to note that the low value for y means that almost all the lift—close to 95%—is generated instantly in the case of a highly swept wing. Thin airfoil theory predicts that only 50% of the lift is instantly generated [11]. The consequence is that unsteady aerodynamic effects are not very significant in this case. The frequency response functions corresponding to indicial functions for quarter-chord sweep angles of 55 and 65 are plotted in Fig. 6 to show how the CE should vary with increasing surface excitation frequency. A range of sweep angles around 60 is shown to give a better understanding of the influence of sweep, especially since the area-weighted averaging approach used to calculate an equivalent sweep for the Half-V is not a standard method, meaning that the true equivalent sweep might be slightly different.

While Fig. 6 shows a decrease in CE with increasing control surface excitation frequency, the effect is relatively small, as the majority of the lift is generated instantly. Unsteady lift build-up accounts for only a minor portion (around 5%) of the total lift. Additionally, the CE curves approach an asymptotic value and show little further reduction beyond approximately 3 Hz. While the unsteady aerodynamics are not very strong, the observed CE parameter inflation strongly contradicts the expected unsteady behavior.

D. Inertial Effects of Structural Vibrations

From Fig. 6, it is observed that the lift CE increases by approximately 12% as the control surface deflection frequency increases from 0.5 to 2.5 Hz. It was hypothesized that this increase is due to the influence of inertial forces acting on the force balance, which are introduced by the wing and its mounting structure. Furthermore, the blue table supporting the entire setup (see Fig. 1) was previously analyzed by LeBlanc et al. [15], who identified a side-to-side rigid-body mode at 5.82 Hz, with a damping ratio of 1.5% and an equivalent spring constant of 2.309e6 N/mm [15]. These dynamic characteristics suggest that the table's response may also influence the force balance measurements.

To investigate the effects of structural dynamics from both the wing and the blue table, a simplified two-degree-of-freedom (2-DoF) model was developed. In this model, the wing (along with its mounting frame) and the blue table (including the force balance) are idealized as mass–spring–damper systems connected in series. The system simulates how the force balance responds when a dynamic lift input is applied to the wing, which is modeled as a

Downloaded by Technische Universiteit Delft on September 21, 2026 | http://arc.aiaa.org | DOI: 10.2514/1.G009651

concentrated force acting on the wing. This single-input single-output system takes the idealized lift as input and produces the measured force at the balance as output. The force balance measurement, F_b, corresponds to the reaction force exerted by the table and depends on the dynamic response—namely, the position and velocity of both the wing and the table. Using only the first mode of the wing was sufficient in this example. The force balance itself is assumed to be much stiffer than the wing and the mounting table; therefore, only its mass is considered. Two additional simplified 1-DoF versions of this model were also created by dropping either the wing or the table from the dynamics.

The state-space representation of the idealized 2-DoF system is provided in Eqs. (6) and (7), where the former defines the state evolution and the latter defines the system output. The states x_1 and x_3 represent the displacements of the wing and table, respectively, while x_2 and x_4 represent their corresponding velocities. The input is the applied lift L, and the output is the measured force F_b. The parameters m, k, and c denote mass, stiffness, and damping, respectively, with subscripts w, t, and b referring to the wing, table, and force balance. The table properties are based on values reported in [15], while the wing parameters were obtained through a ground vibration test (GVT). The first bending mode shape obtained from the GVT has a frequency of 6.65 Hz. A summary of all model parameters is provided in Table 1, with damping values computed from the damping ratio and critical damping. A detailed explanation of the GVT is presented at the end of this section.

$$\begin{bmatrix} \dot{x}_1 \\ \dot{x}_2 \\ \dot{x}_3 \\ \dot{x}_4 \end{bmatrix} = \begin{bmatrix} 0 & 1 & 0 & 0 \\ -\frac{k_w}{m_w} & -\frac{c_w}{m_w} & \frac{k_w}{m_w} & \frac{c_w}{m_w} \\ 0 & 0 & 1 & 0 \\ \frac{k_w}{m_b+m_t} & \frac{c_w}{m_b+m_t} & \frac{-k_w-k_t}{m_b+m_t} & \frac{-c_w-c_t}{m_b+m_t} \end{bmatrix} \begin{bmatrix} x_1 \\ x_2 \\ x_3 \\ x_4 \end{bmatrix} + \begin{bmatrix} 0 \\ \frac{1}{m_w} \\ 0 \\ 0 \end{bmatrix} L \tag{6}$$

$$F_b = \begin{bmatrix} \frac{m_t k_w}{m_b+m_t} & \frac{m_t c_w}{m_b+m_t} & \frac{-m_t k_w+m_b k_t}{m_b+m_t} & \frac{-m_t c_w+m_b c_t}{m_b+m_t} \end{bmatrix} \begin{bmatrix} x_1 \\ x_2 \\ x_3 \\ x_4 \end{bmatrix} + [0]\, L \tag{7}$$

The Bode diagrams of the structural dynamic models are shown in Fig. 7, with the figure showing the magnitude plot zoomed in to the frequency range of interest. Figure 7 shows that the increase in CE observed in the wind tunnel data (red crosses) aligns closely with the prediction of the simplified 2-DoF model, which incorporates the structural properties of both the wing and the mounting table as identified through ground vibration testing. The model that only considers the wing (black curve) also matches well with the results, suggesting that the table dynamics are not as crucial. However, the coupled model was the one used. As the frequency of control surface inputs approaches the first bending mode of the wing, inertial forces amplify the force balance measurements, resulting in an apparent increase in CE estimates if uncorrected force balance data are used. The close match between the model and the parameter inflation observed in the wind tunnel suggests, both qualitatively and quantitatively, that the CE inflation phenomenon is indeed caused by the inertial forces of the vibrating wing being picked up by the force balance.

Table 1 Mass stiffness and damping properties of the wind tunnel setup

Mass	Value	Stiffness	Value	Damping	Value
m_w	32 kg	k_w	56 kN/m	d_w	0.84%
m_t	1670 kg	k_t	2309 kN/m	d_t	1.5%
m_b	55 kg	— —	— —	— —	— —

The GVT was conducted using a Mini SmartShaker from The Modal Shop[**] to excite the structure, while the structural response was measured using a PSV-500 laser scanning vibrometer from Polytec.[††] The input force applied by the shaker was measured using a Model 288D01 mechanical impedance sensor from PCB Piezotronics.[‡‡] The wing was clamped to an aluminum support frame, which was itself fixed to an optical table. The experimental setup is shown in Fig. 8, and the measurement points are in Fig. 9. There are 32 measurement points in total, marked in squares of white tape, but only 3 are highlighted in Fig. 9 for brevity. Figure 10 visualizes the first bending mode shape obtained through the GVT.

The laser vibrometer sequentially scanned 32 points on the wing surface. At each point, the same excitation signal was applied, allowing phase-averaged measurements to be used for computing the frequency response functions (FRFs) at all scan locations.

The wing was excited using a pseudo-random input with a frequency resolution of 39.0625 mHz and a sampling rate of 500 Hz, resulting in 6400 spectral lines per FRF. Each scan at a single point took 25.6 s. To reduce noise, three measurements were taken at each point and averaged. Data acquisition and processing were carried out using PSV software.[§§]

IV. Correction Framework for Control Effectiveness Estimates

So far, this study has outlined the process of identifying CE parameters in wind tunnel tests using dynamic control surface excitations—specifically, multisine and stepped-sine signals on a wing equipped with actuated control surfaces. A new phenomenon, referred to as CE parameter inflation, was observed, and its underlying cause was identified. This section outlines a methodology for correcting force balance measurements by filtering out inertial forces prior to CE parameter estimation.

The general process for correcting wind tunnel force balance measurements for dynamic experiments is illustrated in Fig. 11. The fundamental principle is to identify sources of inertial forces that contaminate force balance measurements and to suppress or remove them using a digital filter that inverts the dynamics of the contributing structural modes. A specially designed filter is only required when the excitation frequencies of interest lie near the structural mode frequencies of the test article or mounting system. In general, this methodology is termed *deconvolution*, with the associated filters called *deconvolution filters*.

A. Correction Filter Design

For the wind tunnel setup considered in this study, the first bending mode of the wing and the side–side rigid-body mode of the mounting table occurred at frequencies close to the actuator excitation band, resulting in measurable inertial contamination of the force balance signals. To correct for this effect, a structural dynamic model of the coupled wing–table system was identified and used to construct a correction filter.

The model was shown to accurately predict the CE parameter inflation observed in the data, as illustrated in Fig. 7. It is formulated as a single-input single-output linear state-space system, which can be converted into a transfer function relating the aerodynamic lift acting on the wing to the force measured by the balance. Inverting this transfer function enables the recovery of the aerodynamic lift by effectively removing inertial contributions from the measured signal. However, the inverted transfer function is improper, making direct implementation as a filter nontrivial. To address this, two approaches are considered: 1) *direct inversion*, in which the improper transfer function is applied in the frequency domain with additional signal conditioning, and 2) *regularized inversion*, where

[**]https://www.modalshop.com/vibration-test/products/vibration-test-shakers/smartshaker-integrated-amp.

[††]https://www.polytec.com/int/vibrometry/products/full-field-vibrometers/psv-500-scanning-vibrometer.

[‡‡]https://www.pcb.com/products?m=288d01.

[§§]https://www.polytec.com/int/vibrometry/products/software/psv-software.

Downloaded by Technische Universiteit Delft on September 21, 2026 | http://arc.aiaa.org | DOI: 10.2514/1.G009651

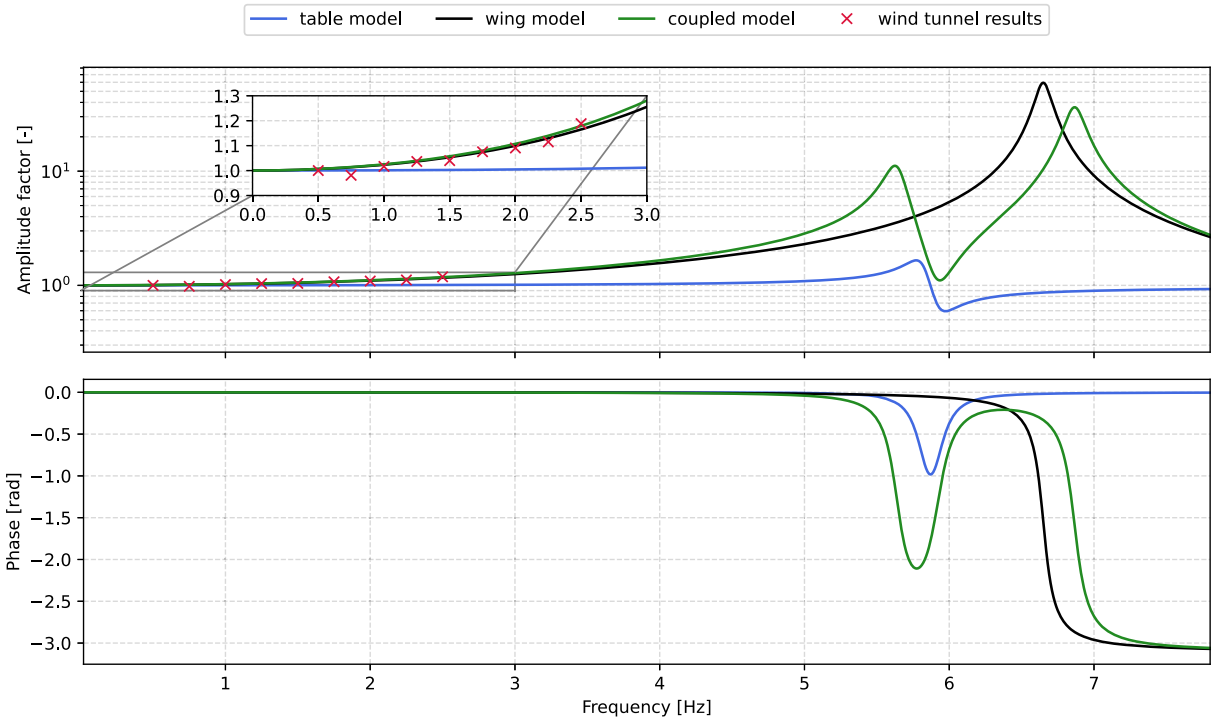


Fig. 7 Bode diagrams of linear state-space models along with wind tunnel results.

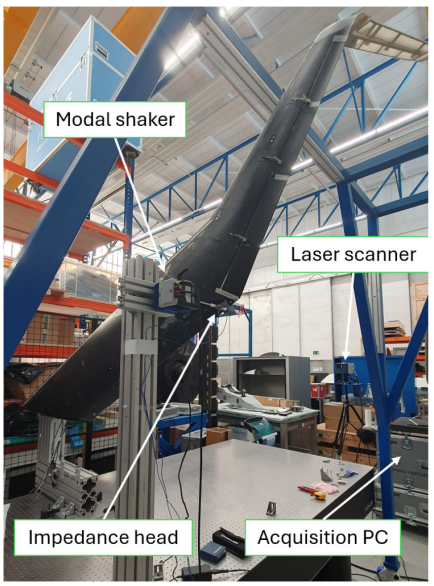


Fig. 8 GVT test setup.



Fig. 9 GVT measurement points (32 total).

a high-frequency pole is introduced at half the sampling frequency to ensure properness while minimizing its impact within the frequency band of interest.

The first approach uses the improper inverted transfer function and applies it in the frequency domain. The Fourier transform of the original force balance signal is computed using a fast Fourier transform, and the negative frequencies are discarded. A numerical frequency response of the inverted transfer function is computed at the frequencies corresponding to those of the transformed signal. Finally, the transformed signal and frequency response are multiplied, and an inverse Fourier transform is applied to the resulting signal, which yields the filtered time-series signal. During this process, half the data are discarded, but linear interpolation of the filtered signal yields a final filtered signal that is the same length as the original.

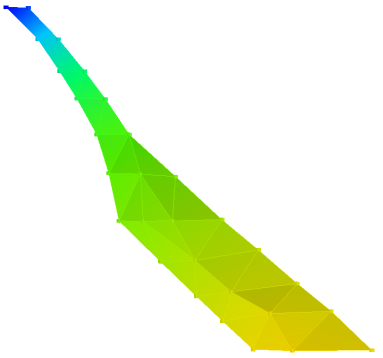


Fig. 10 First bending–torsion mode shape at 6.65 Hz.

Downloaded by Technische Universiteit Delft on September 21, 2026 | http://arc.aiaa.org | DOI: 10.2514/1.G009651

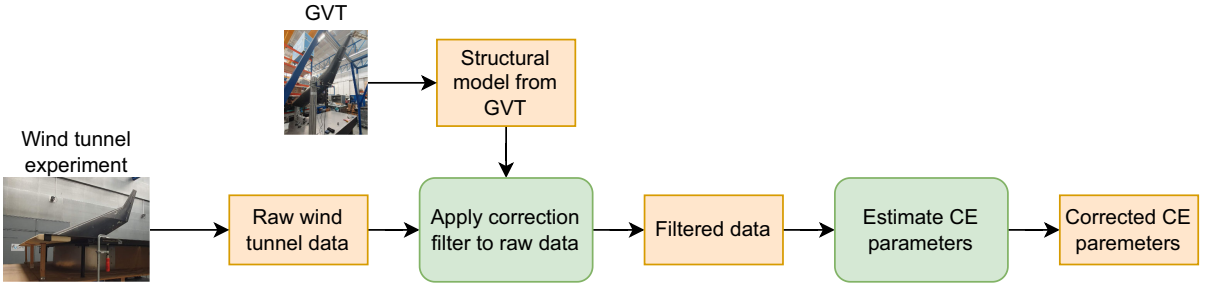


Fig. 11 Data correction framework.

The second approach augments the inverted transfer function by adding an extra pole, ensuring that it becomes a proper transfer function. This pole is placed at 100 Hz, half the sampling frequency of 200 Hz, which is sufficiently far from the structural dynamics frequencies to have a negligible impact on the relevant dynamics. However, introducing this pole results in some phase lag even at lower frequencies.

For both of the approaches mentioned, a low-pass filter with a corner frequency of 10 Hz is also applied to the lift force data measured by the force balance to remove any high-frequency noise. Since the frequencies of the dynamic control surface excitations are never higher than 3.6 Hz in this case, the frequency content in the data above 10 Hz is considered stochastic and not caused directly by surface deflections. Therefore, the use of a low-pass filter is considered valid.

This paper focuses on offline system identification rather than online real-time control (using, for example, incremental nonlinear dynamic inversion control). Therefore, a real-time synchronization filter is not required. Instead, filtering is applied only to the force balance data to remove high-frequency noise caused by aerostructural interactions excited by flow turbulence. The surface deflection is measured directly via potentiometers. In this offline context, the force balance and surface deflection time series are synchronized statically, bypassing the need for the synchronization filters typically used in real-time applications.

B. Applications of Correction Filters to Stepped-Sine Data

Figure 12 presents the CE estimates obtained after applying the correction filter to the raw force balance measurements, using both filter implementation methods. The CE parameters estimated from raw measurements are shown in blue, those obtained from the first filter implementation in green, and those from the second method in orange. The expected unsteady aerodynamic behavior through indicial responses is also shown. The CE estimates obtained from filtered data do not exhibit the inflation phenomenon that was apparent when raw measurements are used.

Figure 13 provides a detailed illustration of how the correction filters improve the accuracy of CE estimates. In this example, the flap deflection input was a pure sinusoid at 2 Hz lasting 10 s, corresponding to the CE estimates at 2 Hz shown in Fig. 12. In all subplots, blue denotes the raw dataset, while green and orange represent the data corrected using methods 1 and 2, respectively. The center plot shows a segment of the lift coefficient time series; the left plot displays a scatter plot of the lift coefficient versus flap deflection for the entire dataset, along with linear fits with slope $C_{L_{\delta_e}}$. The filters' effect is evident in the reduced amplitude of the time series and the lower slope of the fitted lines, indicating smaller CE values. The right subplot shows the distribution of residuals between the data and linear model predictions, with both corrected cases exhibiting reduced error as expected. These results show that both correction methods perform virtually the same.

C. Applications of Correction Filters to Multisine Data

Through the stepped-sine excitations, the efficacy of the correction filters was proven in removing the inertial forces from force balance measurements for dynamic excitations at one frequency. Figure 14 shows the results of applying the correction filters to data acquired through multisine excitations. The top row shows the CE values estimated for each elevon using multisine excitations at varying frequencies, with each data point corresponding to a single

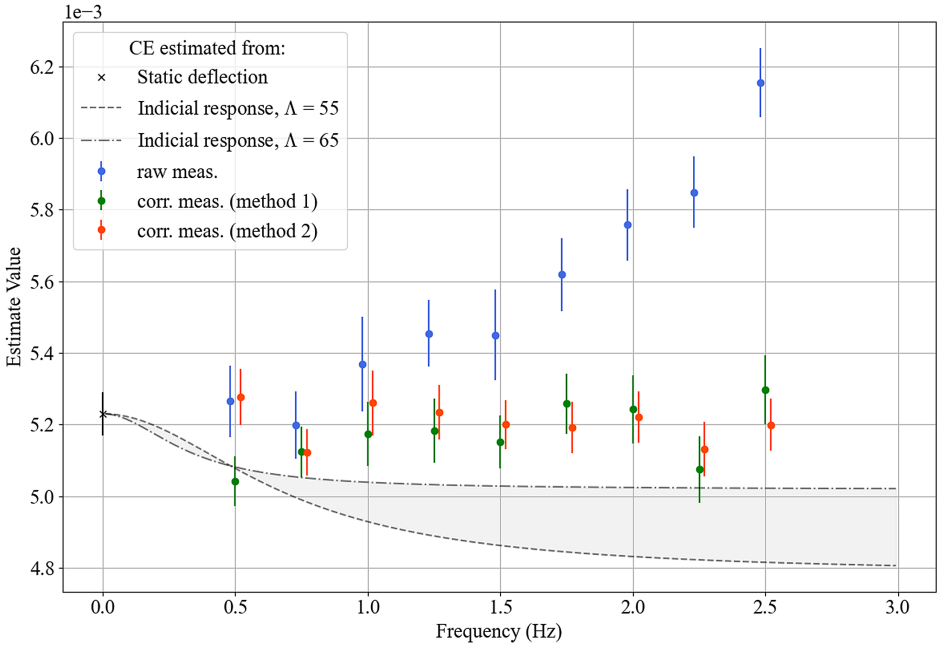


Fig. 12 CE estimated from corrected force balance data.

Downloaded by Technische Universiteit Delft on September 21, 2026 | http://arc.aiaa.org | DOI: 10.2514/1.G009651

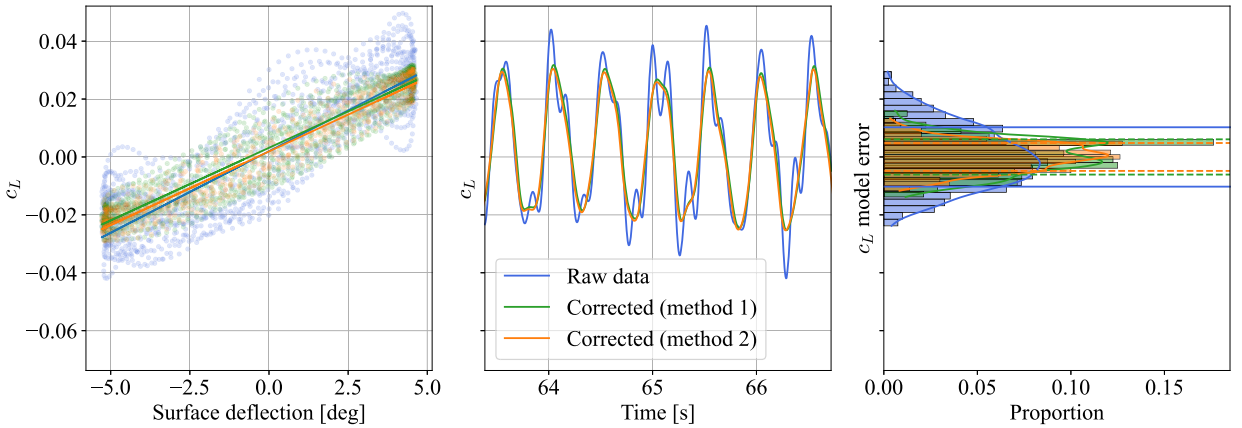


Fig. 13 Correction filters applied at 2 Hz.

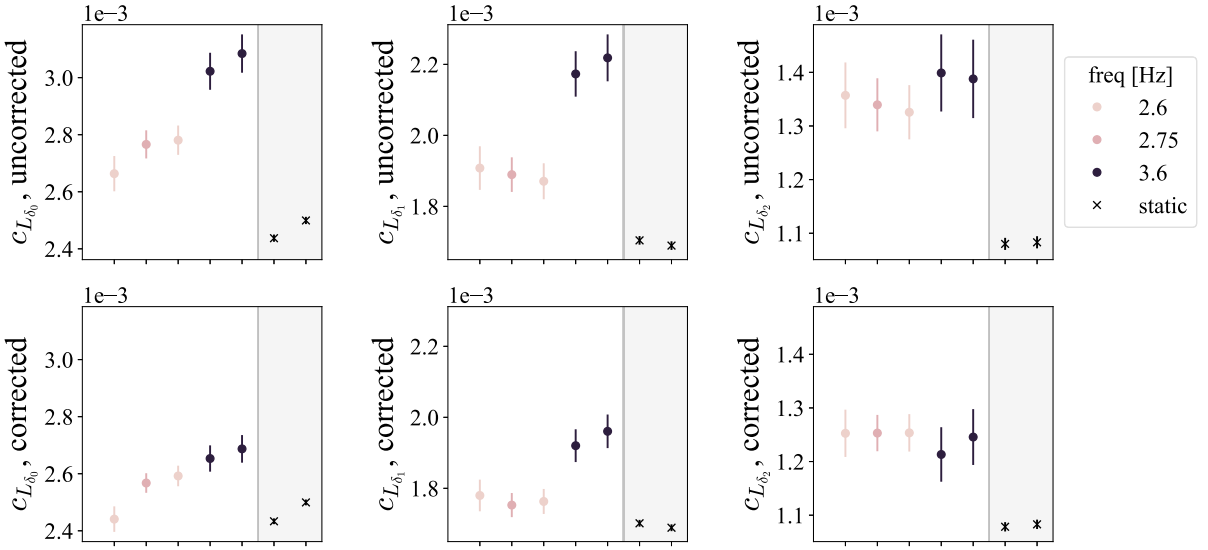


Fig. 14 Application of correction filter to multisine data.

experimental dataset. The bottom row is the same, but the datasets were filtered using method 1, the proper correction filter, before CE values were estimated for each elevon. The CE values obtained from two static experimental runs are also included, as was the case for the stepped-sine excitations shown in Fig. 12; these are included as a reference for what the ground-truth CE estimates should be.

Figure 14 shows that the application of the correction filter reduces the CE estimates from multisine excitations toward those obtained through static tests. However, the dynamic effects due to inertial forces are not completely eliminated. When applied to single-frequency dynamic excitations, the correction filter is able to remove inertial forces such that the CE estimates approach the static values, as was shown through the stepped-sine excitation data in Fig. 12. This will be elaborated upon in the following section.

V. Discussion

While the proposed correction framework demonstrates substantial improvements in the estimation of CE through dynamic excitations, several limitations and open questions remain.

First, although the filtering procedure reduces inertial contamination, the corrected estimates do not perfectly align with unsteady aerodynamic predictions based on indicial response theory. In the present case, the aerodynamic drop-off above 3 Hz is modest (5%), suggesting that inertial effects dominate the discrepancies. However, it remains uncertain whether the indicial-based predictions themselves fully capture the frequency response for this wing geometry. Unsteady aerodynamic effects can be subtle, and their identification is sensitive to both input design and measurement accuracy. Further experiments with well-characterized wings would help to validate whether the corrected force balance truly isolates aerodynamic contributions.

Stepped-sine excitations limited to 2.5 Hz confirmed consistency with static values in that frequency range. However, multisine excitations at 3.6 Hz show that while the corrected CE estimates move closer to the static values, a residual bias remains. The stepped-sine data only allowed the verification of the filter up to 2.5 Hz, with single frequencies being excited. The remaining bias in Fig. 14 indicates that some dynamic contribution is still present after filtering. This is consistent with either incomplete modeling of higher-frequency structural modes or other dynamics not captured by the low-order correction model. While nonlinear interactions may also contribute under simultaneous multifrequency excitation, the present data do not isolate that mechanism, and therefore no definitive attribution is made here.

Second, the methodology assumes that structural and aerodynamic contributions are separable via linear filtering. This assumption is valid when the system is linear, as assumed for the case presented here. For highly flexible wings with low natural frequencies, however, actuator excitations may overlap with structural modes. Strong excitations can cause large structural deflections that lead to geometric nonlinear effects, potentially reducing the applicability of the filter [16–18]. Future work should therefore test the method on flexible configurations where excitation–mode overlap occurs.

Third, the approach depends on accurate knowledge of structural dynamics, which is obtained here through ground vibration testing.

Downloaded by Technische Universiteit Delft on September 21, 2026 | http://arc.aiaa.org | DOI: 10.2514/1.G009651

For general application, a practical recommendation is to characterize the lowest-frequency modes (particularly the first out-of-plane bending mode) either experimentally or via finite-element modeling. This ensures that the correction filter removes inertial effects without attenuating true aerodynamic responses. The sensitivity to the damping ratio is especially important, as lightly damped modes have a stronger influence than highly damped modes away from their natural frequencies.

Finally, it is worth noting that dynamic excitation methods provide benefits beyond static deflection tests. In particular, they enable the exploration of unsteady aerodynamic responses in a frequency-resolved manner, complementing traditional static or quasi-steady estimates. As high-aspect-ratio and flexible wing designs become increasingly relevant, methodologies that combine dynamic excitation with careful correction of inertial effects may become essential for accurate CE characterization. Particularly, with regard to more advanced control techniques that rely on accurate CE estimates, such as incremental nonlinear dynamic inversion control [19–21], the use of this methodology to provide accurate CE estimates can improve controller performance.

VI. Conclusions

This work has identified a previously unreported phenomenon, referred to as control effectiveness (CE) parameter inflation, which arises when inertial forces from structural dynamics contaminate force balance measurements during dynamic control surface excitations in wind tunnel testing. A simple yet effective structural model was used to explain this effect and to design correction filters that mitigate the inertial contribution, yielding more accurate CE estimates. The corrected results confirm that dynamic excitations can provide more reliable CE information while also enabling the study of frequency-dependent aerodynamic effects. As future aircraft configurations become more flexible, such approaches may become increasingly important for aeroelastic modeling and control law development. The methodology and findings presented here offer both a caution against uncorrected dynamic force balance data and a path forward for using dynamic excitations in wind tunnel parameter identification.

Acknowledgments

This publication is part of the project Flying V Flight Control with project number 19511 of the research program Open Technology Programme, which is partly financed by the Dutch Research Council (NWO). The authors would like to acknowledge the in-kind contribution of KLM Royal Dutch Airlines and ADSE.

References

[1] Morelli, E. A., and Klein, V., Aircraft System Identification: Theory and Practice, Vol. 2, Sunflyte Enterprises, Williamsburg, VA, 2016, pp. 95–99, 299, 309–312.

[2] Morelli, E. A., "Multiple Input Design for Real-Time Parameter Estimation in the Frequency Domain," *IFAC Proceedings*, Vol. 36, No. 16, 2003, pp. 639–644. https://doi.org/10.1016/S1474-6670(17)34833-4

[3] Morelli, E. A., "Flight Test Maneuvers for Efficient Aerodynamic Modeling," *Journal of Aircraft*, Vol. 49, No. 6, 2012, pp. 1857–1867. https://doi.org/10.2514/1.C031699

[4] Morelli, E. A., "Optimal Input Design for Aircraft Stability and Control Flight Testing," *Journal of Optimization Theory and Applications*, Vol. 191, Nos. 2–3, 2021, pp. 415–439. https://doi.org/10.1007/s10957-021-01912-0

[5] Morelli, E. A., "Practical Aspects of Multiple-Input Design for Aircraft System Identification Flight Tests," *AIAA Aviation 2021 Forum*, AIAA Paper 2021-2795, 2021. https://doi.org/10.2514/6.2021-2795

[6] Grauer, J. A., and Boucher, M. J., "Aircraft System Identification From Multisine Inputs and Frequency Responses," *Journal of Guidance, Control, and Dynamics*, Vol. 43, No. 12, 2020, pp. 2391–2398. https://doi.org/10.2514/1.G005131

[7] Grauer, J. A., and Boucher, M. J., "Real-Time Estimation of Bare-Airframe Frequency Responses From Closed-Loop Data and Multisine Inputs," *Journal of Guidance, Control, and Dynamics*, Vol. 43, No. 2, 2020, pp. 288–298. https://doi.org/10.2514/1.G004574

[8] Grauer, J. A., "Frequency Response Estimation for Multiple Aircraft Control Loops Using Orthogonal Phase-Optimized Multisine Inputs," *Processes*, Vol. 10, No. 4, 2022, p. 619. https://doi.org/10.3390/pr10040619

[9] Heeg, J., and Morelli, E., "Evaluation of Simultaneous Multisine Excitation of the Joined Wing Aeroelastic Wind Tunnel Model," *52nd AIAA/ASME/ASCE/AHS/ASC Structures, Structural Dynamics and Materials Conference 19th AIAA/ASME/AHS Adaptive Structures Conference 13t*, AIAA Paper 2011-1959, 2011. https://doi.org/10.2514/6.2011-1959

[10] Ertveldt, J., Pintelon, R., and Vanlanduit, S., "Identification of Unsteady Aerodynamic Forces from Forced Motion Wind Tunnel Experiments," *AIAA Journal*, Vol. 54, No. 10, 2016, pp. 3265–3273. https://doi.org/10.2514/1.J054773

[11] Theodorsen, T., "General Theory of Aerodynamic Instability and the Mechanism of Flutter," NACA TR 496, 1934.

[12] Wagner, H., "Über die Entstehung des dynamischen Auftriebes von Tragflügeln," *ZAMM-Journal of Applied Mathematics and Mechanics/ Zeitschrift für Angewandte Mathematik und Mechanik*, Vol. 5, No. 1, 1924, pp. 17–35. https://doi.org/10.1002/zamm.19250050103

[13] García, A. R., Brown, M., Atherstone, D., Arnhem, N.v, and Vos, R., "Aerodynamic Model Identification of the Flying V From Sub-Scale Flight Test Data," *AIAA SciTech Forum 2022*, AIAA Paper 2022-0713, 2022. https://doi.org/10.2514/6.2022-0713

[14] Queijo, M., Wells, W. R., and Keskar, D. A., "Approximate Indicial Lift Function for Tapered, Swept Wings in Incompressible Flow," NASA TP 1241, Aug. 1978.

[15] LeBlanc, B., and Ferreira, C., "Experimental Characterization of H-VAWT Turbine for Development of a Digital Twin," *Journal of Physics: Conference Series*, Vol. 1452, No. 1, 2020, Paper 012057. https://doi.org/10.1088/1742-6596/1452/1/012057

[16] Riso, C., and Cesnik, C. E. S., "Geometrically Nonlinear Effects in Wing Aeroelastic Dynamics at Large Deflections," *Journal of Fluids and Structures*, Vol. 120, July 2023, Paper 103897. https://doi.org/10.1016/j.jfluidstructs.2023.103897

[17] Perroni, A. P., and Bussamra, F. L. S., "Effects of Geometric Nonlinearity on Flexible Wing Structures," *Journal of Aircraft*, Vol. 58, No. 1, 2021, pp. 85–97. https://doi.org/10.2514/1.C035745

[18] Afonso, F., Vale, J., Oliveira, E., Lau, F., and Suleman, A., "A Review on Non-Linear Aeroelasticity of High Aspect-Ratio Wings," *Progress in Aerospace Sciences*, Vol. 89, Feb. 2017, pp. 40–68. https://doi.org/10.1016/j.paerosci.2016.12.004

[19] Sieberling, S., Chu, Q., and Mulder, J., "Robust Flight Control Using Incremental Nonlinear Dynamic Inversion and Angular Acceleration Prediction," *Journal of Guidance, Control, and Dynamics*, Vol. 33, No. 6, 2010, pp. 1732–1742. https://doi.org/10.2514/1.49978

[20] Smeur, E. J. J., Chu, Q., and de Croon, G. C. H. E., "Adaptive Incremental Nonlinear Dynamic Inversion for Attitude Control of Micro Air Vehicles," *Journal of Guidance, Control, and Dynamics*, Vol. 39, No. 3, 2016, pp. 450–461. https://doi.org/10.2514/1.G001490

[21] Wang, X., van Kampen, E.-J., Chu, Q., and Lu, P., "Stability Analysis for Incremental Nonlinear Dynamic Inversion Control," *Journal of Guidance, Control, and Dynamics*, Vol. 42, No. 5, 2019, pp. 1116–1129. https://doi.org/10.2514/1.G003791

V. Mukhopadhyay
Associate Editor

Downloaded by Technische Universiteit Delft on September 21, 2026 | http://arc.aiaa.org | DOI: 10.2514/1.G009651